An Equivalent Circuit Model for a Ge Waveguide Photodetector on Si

Jeong-Min Lee, *Student Member, IEEE*, Seong-Ho Cho, and Woo-Young Choi, *Member, IEEE*

***Abstract*— We present an equivalent circuit model with improved accuracy for 1.5-μm germanium waveguide-type vertical photodetectors on a silicon-on-insulator substrate. Our model consists of passive circuit components, two current sources for photogenerated carrier transports, and one noise current source. Model parameters are extracted from electrical S-parameter measurements, TCAD simulations of photodetection frequency responses, and noise measurements. The resulting equivalent circuit model accurately provides photodetection frequency responses at different bias voltages and should be of great use for high-performance optical receiver circuit design.**

***Index Terms*— Silicon photonics, germanium photodetector equivalent circuit, photodetector noise, photodetection frequency response.**

I. INTRODUCTION

SILICON photonics is attracting a great amount of research interests as it can realize highly integrated photonic circuits based on mature silicon processing technology and provide solutions for the interconnect bottleneck of high-performance electronic systems [1]. The photodetector (PD) is one of the key devices for realizing integrated photonic circuits, and high-performance germanium photodetectors (Ge-PDs) that can detect 1.5-μm wavelength light can be realized with silicon processing technology. High-speed waveguide-type Ge-PDs on Si [2]–[4] as well as high-performance integrated optical receivers containing these PDs [5], [6] have been reported.

An accurate equivalent circuit model for a PD can explain the influence of various PD device parameters on PD performances [7], [8]. Furthermore, such a model is very useful for optimal designing of high-frequency and high-sensitivity optical receivers. For example, in order to realize high-sensitive and low-power optical receivers with advanced CMOS technology, the precise knowledge and optimization of Ge-PD junction capacitance is essential [9]–[12].

Photodetection frequency responses are usually limited by device *RC* time constant and photogenerated carrier transit time, and the equivalent circuit model shown in Fig. 1(a) is often used [13], where C_{j} and R_{j} are the junction capacitance and resistance, respectively, R_{s} is the series resistance and the current source represents photogenerated carriers. Z_{para} is added in the Fig. 1(a) in order to account for the influence of various parasitic elements including pads and interconnects. However, this model cannot accurately model photodetection frequency responses observed for several waveguide Ge-PDs [13]–[15], especially at low-frequencies where the measured responses show a clear roll-off. For example, Fig. 1(b) shows the measured photodetection frequency response for our Ge-PD whose structure is shown in Fig. 2(a) and (b) along with the simulated response using the model given in Fig. 1(a). For this simulation, circuit parameter values are determined from measurement, details of which are given in Section III, and a single-pole frequency response is assumed for the current source. We have previously identified that this discrepancy is due to the diffusion of photogenerated carriers in the intrinsic Ge region where the electric field is not sufficiently large and adding another current source for this diffusion component provides better agreement between measurement and simulation [16].

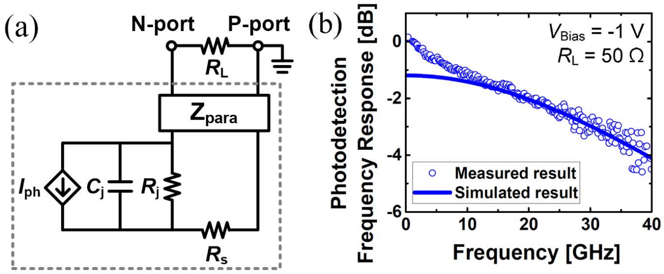

Fig. 1. (a) Equivalent circuit model for PD with one photogenerated-carrier current source and (b) measured and simulated photodetection frequency responses of Ge-PD.

In this letter, we present an accurate equivalent circuit model for the waveguide-type Ge-PD. Our model has two current sources for photogenerated carriers, one for those carriers experiencing drift and the other diffusion. Although the circuit model itself is similar to the model used in our previous report [16], we introduce a new technique for accurate extraction of model parameters for the current sources representing photogenerated carriers based on TCAD and 3-D FDTD simulation. Furthermore, our model contains the noise current source that represents the Ge-PD noise characteristics. We also demonstrate that, using our model, we can identify the influence of various different time constants in the Ge-PD on its frequency response characteristics.

II. DEVICE STRUCTURE

Fig. 2(a) and (b) show the top-view and cross-section of the vertical Ge-PD investigated in this letter. It was fabricated on 220-nm thick Silicon-on-Insulator layer having 2-μm thick buried-oxide layer (BOX) through IME silicon photonics multi-project wafer service. The device is composed of highly

---

Manuscript received June 30, 2016; accepted August 1, 2016. Date of publication September 20, 2016; date of current version October 11, 2016. This work was supported by the National Research Foundation of Korea through the Korean Government under Grant 2015R1A2A2A01007772.

J.-M. Lee and W.-Y. Choi are with the Department of Electrical and Electronic Engineering, Yonsei University, Seoul 120-749, South Korea (e-mail: wchoi@yonsei.ac.kr).

S.-H. Cho is with the Samsung Advanced Institute of Technology, Suwon 443-803, South Korea.

Color versions of one or more of the figures in this letter are available online at http://ieeexplore.ieee.org.

Digital Object Identifier 10.1109/LPT.2016.2598369

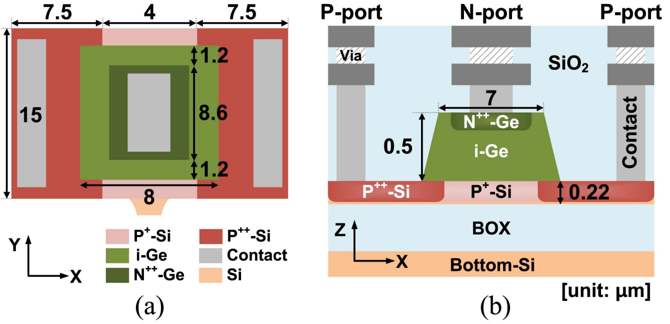

Fig. 2. (a) Top-view and (b) cross-section of Ge-PD.

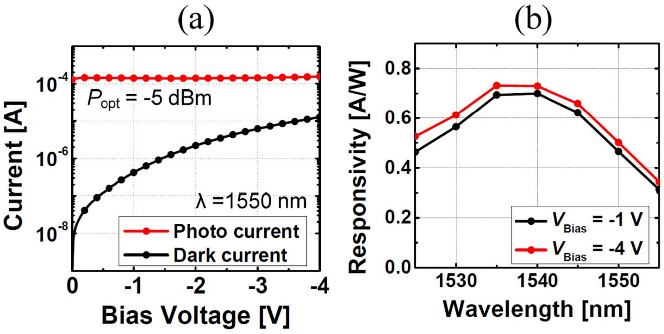

Fig. 3. (a) Measured I-V and (b) responsivity-wavelength characteristics.

n-doped Ge (N^{++}-Ge) layer, 0.5-μm thick intrinsic Ge (i-Ge) layer, and 0.22-μm thick p-doped Si (P^{+}-Si and P^{++}-Si) layer. It is nominally 7-μm wide on the top, 8-μm wide at the bottom, and 11-μm long. The peak nominal doping concentrations are 1.27×10^{21} cm^{-3} for N^{++}-Ge, 3.5×10^{19} cm^{-3} for P^{+}-Si, and 5×10^{20} cm^{-3} for P^{++}-Si. This Ge-PD is similar to the device investigated in [16], but the dimension for the bottom P^{+}-Si region is reduced from 12 to 4 μm so that series resistance is decreased from 130 to 88 Ω and, consequently, its photodetection bandwidth is enhanced from 22 to 32 GHz at -1 V. Fig. 3(a) and (b) show measured current-voltage characteristics and measured responsivities for different wavelengths at two different reverse bias voltages, respectively. Since our target application is 1550 nm, our modeling efforts in this letter are focused at 1550 nm.

In order to identify the regions where photogenerated carriers transport by diffusion, we simulated the electron-hole pair generation rate due to absorption of the input light inside the waveguide Ge-PD using Lumerical 3-D FDTD and the electric-field distribution within the device using TCAD Sentaurus. The results are shown in Fig. 4(a) for the generation rate and Fig. 4(b) for the electric-field profile at -1 V. As can be seen in Fig. 4(b), there is a region in the front and back side of the device, where the electric field is not strong. This is because top N^{++}-Ge layer has to be at least 1.2-μm away from i-Ge layer by the design rule. It can be also seen in Fig. 4(a) that a fair amount of light gets absorbed in the front side of the device where there is no strong electric field. Those carriers generated in this region do not experience drift and have to transport by diffusion.

III. GE-PD EQUIVALENT CIRCUIT MODEL

Fig. 5(a) shows our equivalent circuit model for the Ge-PD. I_1 represents photogenerated carriers experiencing diffusion and I_2 drift. The frequency response of I_1 and I_2 can be modeled by a single time constant, τ_1 for I_1 and τ_2 for I_2, along with corresponding DC gain, A_1 and A_2, sum of which represents Ge-PD DC responsivity but is normalized to one for simplicity in this letter. Fig. 5(b) graphically shows the frequency responses of $I_1(f)$ and $I_2(f)$. Our model also contains the noise current source I_n for the noises generated in the Ge-PD due to three different mechanisms shown in Fig. 5(c). Z_{para} represents parasitic components due to the pads and interconnects, which must be considered for accurate modeling of Ge-PD dynamics. As shown in Fig. 5(a), $R_{\text{int,p}}$, $R_{\text{int,n}}$ and $L_{\text{int,p}}$, $L_{\text{int,n}}$ represent parasitic resistances and inductances in the interconnects from P-port and N-port to the bottom metal layer, respectively. C_{pad} represents the parasitic capacitance between P- and N-port pads and $C_{\text{c-c}}$ is the capacitance between Ge-PD metal contacts. For simplicity, we model these parasitic elements together with Z_{para} shown in inset of Fig. 5(a), in which $R_{\text{int}} = R_{\text{int,p}} + R_{\text{int,n}}$ and $L_{\text{int}} = L_{\text{int,p}} + L_{\text{int}}$.

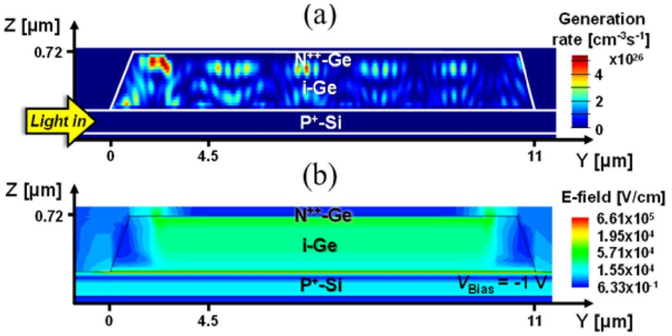

Fig. 4. Simulated (a) 3D-FDTD generation-rate profile and (b) electric-field profile at -1 V within Ge-PD.

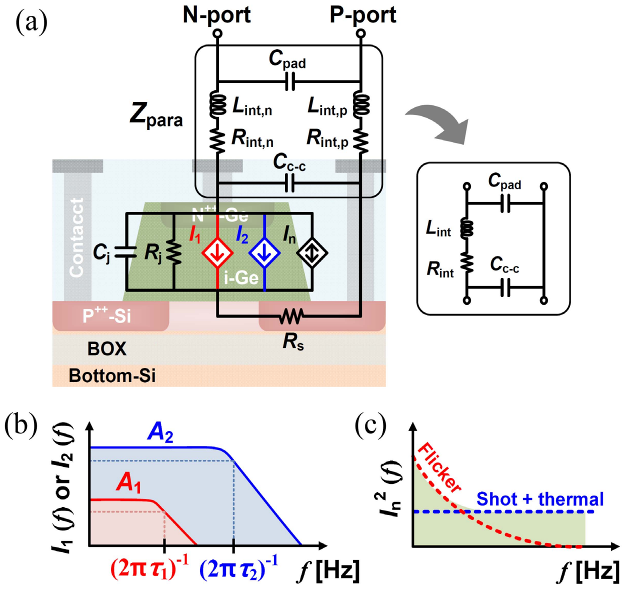

Fig. 5. (a) A modified equivalent circuit model of Ge-PD, (b) frequency responses of photogenerated currents and (c) noise characteristics.

In order to extract R_{int}, L_{int}, and C_{pad}, open and short test patterns are implemented on the same die, and their electrical S-parameters are measured from 100 MHZ to 40 GHz using a vector network analyzer and converted into Y- and Z-parameters. From real and imaginary parts of those

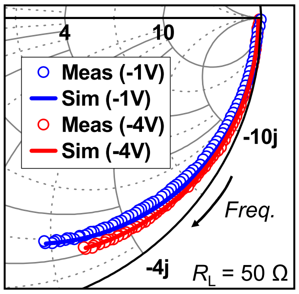

Fig. 6. Measured and simulated reflection coefficients for Ge-PD from 100 MHZ to 40 GHz at −1 and −4 V.

TABLE I

EXTRACTED RC PARAMETERS AND RC TIME CONSTANT

	–1 V	–4 V
R_s [Ω]	88	
C_j [fF]	15.9	11.6
R_j [kΩ]	20	
$C_{c\text{-}c}$ [fF]	6	
τ_{RC} [ps]	2.15	1.59

parameters, values for C_{pad}, R_{int}, and L_{int} are determined as 4.35 fF, 1.1 Ω, and 65 pH, respectively. R_s, C_j, R_j, and $C_{c\text{-}c}$ are extracted by measuring electrical reflection coefficients of the Ge-PD and fitting the simulation based on these parameters to the measurement results. Fig. 6 shows measured and simulated reflection coefficients at two different bias voltages and Table I gives the extracted numerical values that are used for simulation.

In order to determine model parameter values for I_1 and I_2, the doping profiles within our Ge-PD are simulated in TCAD with the doping process information provided by the foundry service, and an accurate 3-D model of the doping profile within our Ge-PD is realized in TCAD. Then, spatial distribution of the optical generation rates, which represent photogenerated electron and hole concentrations, are determined with Lumerical 3-D FDTD simulation and imported into TCAD after meshes are carefully matched between 3-D FDTD and TCAD simulation. Then, we are able to perform photodetection frequency response simulation for our Ge-PD in TCAD, results of which agree well with the measurement.

For extracting model parameters for diffusing and drifting photogenerated carriers, two virtual generation profiles are created, one containing the generation rates only in the region where the electric field is small (less than 4500 V/cm) as shown in Fig. 7(a) where carriers experience diffusion, and the other only in the region where the electric field is strong (larger than 4500 V/cm) where carriers experience drift as shown in Fig. 7(b). It was empirically found that our results do not change much as long as the diffusion/drift boundary field value is between 4000-V/cm and 5000-V/cm. Then, we can simulate in TCAD the photodetection frequency responses for each case and obtain separate frequency responses for diffusing and drifting photogenerated carriers. Hollow circles in Fig. 7(c) and (d) show such simulated frequency responses at −1 and −4 V, respectively. From these, we can easily determine values for A_1, τ_1 for I_1 and A_2, τ_2 for I_2 that produce the best matching between TCAD simulation and single-pole response. Table II shows these values. Both A_1 and τ_1 are smaller for larger reverse bias voltage as can be seen in Table II because with the larger reverse bias voltage photogenerated carriers experience diffusion within a smaller portion of the device and, consequently, need to diffuse a smaller distance. τ_2 does not change with bias voltages because carriers drift with the saturation velocity, which does not change much with the bias voltages.

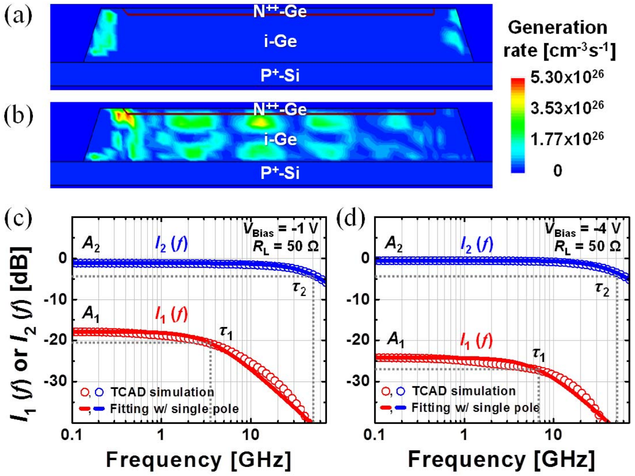

Fig. 7. Generation-rate profiles of (a) diffusion and (b) drift photogenerated carriers at −1 V, and simulated frequency responses for two current source models at (c) −1 and (d) −4 V.

TABLE II

EXTRACTED PARAMETERS FOR TWO CURRENT SOURCES

	−1 V	−4 V
τ_1 [ps]	43.0	23.4
A_1 [%]	12.7	6.2
τ_2 [ps]	3.12	
A_2 [%]	87.3	93.8

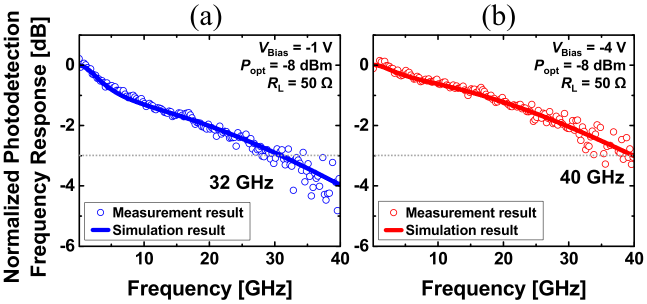

Fig. 8. Measured and simulated photodetection frequency responses from 100 MHZ to 40 GHz for Ge-PD at (a) −1 and (b) −4 V.

Fig. 8(a) and (b) show the simulation results at −1 and −4 V for the complete Ge-PD equivalent circuit along with the measured results. For the measurement, 1550-nm CW light is injected into the Ge-PD through the on-chip grating coupler with a lensed fiber and a lightwave component analyzer is used.

For noise characterization, the Ge-PD noise spectral density is measured at room temperature with a spectrum analyzer. Since the measurement sensitivity of our spectrum analyzer is not high enough for measuring Ge-PD noises, two commercially available low-noise amplifiers (LNAs) having 62-dB gain and 3-dB noise figure are used in cascade in order to boost the noise level and calibrated out. A very careful calibration is done for all the components used in the measurement.

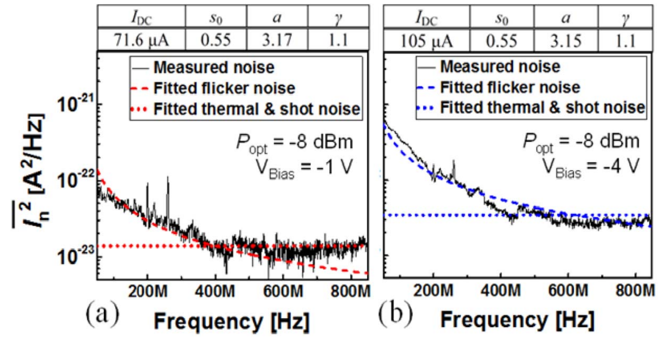

Fig. 9. Measured and fitted noise spectral densities of Ge-PD and their fitting parameters at (a) −1 and (b) −4 V.

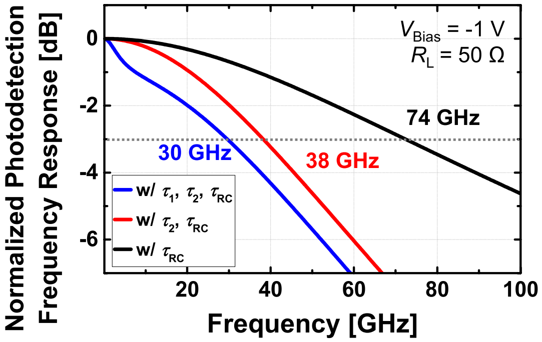

Fig. 10. Simulated photodetection frequency responses for Ge-PD at −1 V with different combination of diffusion (τ_1), drift (τ_2), and *RC* time constant (τ_{RC}).

Fig. 9(a) and (b) show the measured noise spectral densities from 50 to 850 MHZ at −1 and −4 V under −8-dBm optical power.

The measured noise spectral density can be fitted with [17]

$$\overline{I_n^2} = s_0 \frac{I_{DC}^a}{f^\gamma} + 2qI_{DC} + \frac{4kT}{R_j} \qquad (1)$$

where $\overline{I_n^2}$ is the noise spectral density, I_{DC} is the DC photocurrent, s_0, a, γ are fitting parameters, q is the electron charge, k is the Boltzmann constant, T is the temperature in K, and R_j is the junction resistance extracted in Table I. As shown in (1), the Ge-PD noise spectral density consists of the spectrally-dependent flicker noise dominant at low frequencies and the constant shot and thermal noises dominant at high frequencies [17]. Fig. 9(a) and (b) also show the fitted noise spectral densities using (1) and numerical values for fitting parameters are given in insets.

IV. PHOTODETECTION FREQUENCY RESPONSE ANALYSIS

With the equivalent circuit model, we can identify how each of three time constants (*RC*, diffusion, and drift) influences the photodetection frequency response. Fig. 10 shows the simulated photodetection frequency responses based on our equivalent circuit model at −1 V considering all three time constants (blue line), only τ_2 and τ_{RC} or $A_1 = 0$ (red line), and only τ_{RC} (black line). Z_{para} are not included for these simulations since we want to consider only the Ge-PD core dynamics. It is interesting to note that the photodetection bandwidth is slightly higher with Z_{para} (32 GHz) than without (30 GHz). This is because the inductor in Z_{para} provides a small amount of frequency peaking. For $A_1 = 0$, the photodetection 3-dB bandwidth goes up to 38 GHz, indicating that the diffusion of photogenerated carriers reduces the photodetection bandwidth by about 20 %. Furthermore, we can clearly see that carrier transport rather than τ_{RC} is the bandwidth limiting factor for our Ge-PD. This gives a clear design guideline for further bandwidth enhancement of Ge-PD.

V. CONCLUSION

We present an equivalent circuit model for a Ge-PD fabricated on Si. Our model includes passive circuit elements and two current sources for photogenerated carriers experiencing diffusion and drift and a noise current source. We successfully extract accurate values for our model parameters based on measurement and simulation. Our model should be very useful for identifying the influence of various device parameters on the Ge-PD performance and designing high-performance optical receivers based on our Ge-PD.

REFERENCES

[1] M. Haurylau *et al.*, "On-chip optical interconnect roadmap: Challenges and critical directions," *IEEE J. Sel. Topics Quantum Electron.*, vol. 12, no. 6, pp. 1699–1705, Nov./Dec. 2006.

[2] G. Dehlinger, S. J. Koester, J. D. Schaub, J. O. Chu, Q. C. Ouyang, and A. Grill, "High-speed germanium-on-SOI lateral PIN photodiodes," *IEEE Photon. Technol. Lett.*, vol. 16, no. 11, pp. 2547–2549, Nov. 2004.

[3] A. Novack *et al.*, "Germanium photodetector with 60 GHz bandwidth using inductive gain peaking," *Opt. Exp.*, vol. 21, no. 23, pp. 28387–28393, Nov. 2013.

[4] S. Assefa *et al.*, "CMOS-integrated high-speed MSM germanium waveguide photodetector," *Opt. Exp.*, vol. 18, no. 5, pp. 4986–4999, Feb. 2010.

[5] J. F. Buckwalter, X. Zheng, G. Li, K. Raj, and A. V. Krishnamoorthy, "A monolithic 25-Gb/s transceiver with photonic ring modulators and Ge detectors in a 130-nm CMOS SOI process," *IEEE J. Solid-State Circuits*, vol. 47, no. 6, pp. 1309–1322, Jun. 2012.

[6] H. Pan *et al.*, "High-speed receiver based on waveguide germanium photodetector wire-bonded to 90 nm SOI CMOS amplifier," *Opt. Exp.*, vol. 20, no. 16, pp. 18145–18155, Jul. 2012.

[7] M.-J. Lee and W.-Y. Choi, "Area-dependent photodetection frequency response characterization of silicon avalanche photodetectors fabricated with standard CMOS technology," *IEEE Trans. Electron Devices*, vol. 60, no. 3, pp. 998–1004, Mar. 2013.

[8] M.-J. Lee, H.-S. Kang, and W.-Y. Choi, "Equivalent circuit model for Si avalanche photodetectors fabricated in standard CMOS process," *IEEE Electron Device Lett.*, vol. 29, no. 10, pp. 1115–1117, Oct. 2008.

[9] J. Li and J. Buckwalter, "Energy efficiency of optoelectronic interfaces in scaled FinFET and SOI CMOS technologies," in *Proc. OIC*, 2015, pp. 18–19.

[10] M. Georgas, J. Leu, B. Moss, C. Sun, and V. Stojanović, "Addressing link-level design tradeoffs for integrated photonic interconnects," in *Proc. CICC*, Sep. 2011, pp. 1–8.

[11] J. Li, X. Zheng, A. V. Krishnamoorthy, and J. F. Buckwalter, "Scaling trends for picojoule-per-bit WDM photonic interconnects in CMOS SOI and FinFET processes," *J. Lightw. Technol.*, vol. 34, no. 11, pp. 2730–2742, Jun. 1, 2016.

[12] F. Liu *et al.*, "10 Gbps, 530 fJ/b optical transceiver circuits in 40 nm CMOS," in *Proc. VLSIC*, 2011, pp. 290–291.

[13] M. Gould, T. Baehr-Jones, R. Ding, and M. Hochberg, "Bandwidth enhancement of waveguide-coupled photodetectors with inductive gain peaking," *Opt. Exp.*, vol. 20, no. 7, pp. 7101–7111, Mar. 2012.

[14] H. T. Chen *et al.*, "High-responsivity low-voltage 28-Gb/s Ge p-i-n photodetector with silicon contacts," *J. Lightw. Technol.*, vol. 33, no. 4, pp. 820–824, Feb. 15, 2015.

[15] T.-Y. Liow *et al.*, "Silicon optical interconnect device technologies for 40 Gb/s and beyond," *IEEE J. Sel. Topics Quantum Electron.*, vol. 19, no. 2, Mar./Apr. 2013, Art. no. 8200312.

[16] J.-M. Lee and W.-Y. Choi, "An equivalent circuit model for germanium waveguide vertical photodetectors on Si," in *Proc. MWP/APMP*, 2014, pp. 139–141.

[17] N. C. Harris, T. Baehr-Jones, A. E.-J. Lim, T. Y. Liow, G. Q. Lo, and M. Hochberg, "Noise characterization of a waveguide-coupled MSM photodetector exceeding unity quantum efficiency," *J. Lightw. Technol.*, vol. 31, no. 1, pp. 23–27, Jan. 1, 2013.